

A Conductive and Anti-Freezing PC-OH Organic Hydrogel with High Adhesion and Self-Healing Activities for Wearable Electronics

Zhenglin Chen^{1,2,3#}, Jiaqi Yang^{4#}, Zhicheng Du^{1,2,3#}, Likun Zhang^{1,2,3}, Haifei Guan^{1,2,3}, Zhengyang Lei^{1,2,3}, Xiaopeng Zhang^{1,2,3}, Canhui Yang⁵, Ying Zhu^{1,2,3}, Qianhui Sun^{1,2,3}, Lulu Xu^{1,2,3}, Ke Lin^{1,2,3}, Yuchen Wang^{1,2,3}, Chuhui Wang^{1,2,3}, Chong Zhang³, Dongmei Yu^{6*}, Peiwu Qin^{1,2,3*}, Can Yang Zhang^{1,2,3*}

¹Institute of Biopharmaceutics and Health Engineering, Tsinghua Shenzhen International Graduate School, Shenzhen 518055, China

²Shenzhen Bay Laboratory, Shenzhen 518107, China.

³Key Laboratory of Industrial Biocatalysis, Ministry of Education; Tsinghua University, Beijing 100084, China

⁴State Key Laboratory of Urban Water Resources and Environment, School of Civil & Environmental Engineering, Harbin Institute of Technology (Shenzhen), Shenzhen 518055, China

⁵Soft Mechanics Lab, Department of Mechanics and Aerospace Engineering, Southern University of Science and Technology, Shenzhen 518055, China

⁶School of Mechanical, Electrical & Information Engineering, Shandong University, Weihai 264209, China

#These authors contributed equally to this work.

*Corresponding authors.

E-mail: [\(D. Yu\);](mailto:yudongmei@sdu.edu.cn) [\(P. Qin\);](mailto:pwqin@sz.tsinghua.edu.cn) [\(C.Y. Zhang\).](mailto:zhang.cy@sz.tsinghua.edu.cn)

Abstract

In the realm of flexible wearable electronics and interactive technologies, the adhesive and touch-sensing properties of materials play a crucial role, especially soft ionic conductors. However, these materials face several challenges in practical application, including structural damage, loss of functionality, and device stratification, particularly in extreme environments. Herein, a novel multifunctional organic hydrogel, known as PC-OH, was designed and prepared with improved performances. This hydrogel exhibits remarkable adhesion capabilities to different materials, including plastics, paper, glass, and human skin even underwater. The PC-OH hydrogel shows high self-healing capability for enhancing its durability. Furthermore, this PC-OH hydrogel shows conductive and anti-freezing over a wide temperature range, as well as high stretchable and stability. Moreover, PC-OH hydrogel-based surface capacitive touch system has been developed with impressive touch-sensing abilities, allowing for precise position detection, even in wet and fluctuating temperature conditions. The wearable touch panel has been successfully demonstrated through the ability to write text, draw figures, and play electronic games, showcasing its potential use in various applications. Overall, the PC-OH organic hydrogel holds great potential applications in wearable electronics, offering solutions to longstanding challenges in adhesion and touch-sensing.

Introduction

Integrated touch panels are crucial components in the interaction between human-machine interfaces and displays due to their simplicity, portability, and intuitiveness. Various touch panel technologies have been reported, such as capacitive [1–5], resistive [6], optical [7], surface acoustic wave [8,9], bending wave [10], piezoelectric [11], and triboelectric (TENG) mechanisms [12,13]. Capacitive touch sensing is widely employed in electronic devices like smartphones, portable computers, gaming consoles, and ticket machines. However, next-generation touch panels demand more important properties such as biocompatibility, stretchability, softness, environmental stability, self-healing, and self-adhesion, which conventional panels like capacitive ones cannot afford due to their inherent stiffness and brittleness [14,15]. To address these challenges, researchers have investigated alternative materials such as metal composites [16], carbon nanomaterials [17], conducting polymers [1,18], and metal nanowires [19]. However, these materials face their own shortness including dramatic sheet resistance increase when stretching, and poor self-healing ability [20]. Furthermore, biocompatibility is becoming a progressively important feature for these alternative materials [21–25]. Therefore, conductive hydrogels have attracted considerable attention due to their versatility, transparency, scalability, biocompatibility, and electrical conductivity, making them a valid candidate for next-generation touch panels. Conductive hydrogels have been widely studied and extensively used in many fields, including tactile/strain sensors [26,27], diodes/transistors [28,29], human-machine interfaces (*e.g.*, flexible keyboards [30] and touch panels [2–5]), alternating-current electroluminescent devices (ACEL) [31,32], the actuator [33–36], energy harvesting/storage devices [35,37] and soft robotics [38].

However, hydrogel electronics are susceptible to temperature-induced changes in conductivity and sensing [1,39,40]. Sub-zero temperatures lead to the loss of stretchability, conductivity, self-healing, and self-adhesion properties [39–46]. In ion hydrogels, the freezing process reduces the number of free water molecules, resulting in a slow ion migration rate [46,47], which leads to functional deterioration and signal inaccuracy. This inherent deficiency limits the practical application at low temperatures. Long-term use can also affect the mechanical properties of the hydrogels due to dehydration. Moreover, under specific conditions (*e.g.* wet, cold, dry, continuous deformation), adhesion to

substrates can weaken, potentially leading to delamination and reduced data reliability. This necessitates the use of additional adhesives like bandages, 3M adhesives, or scotch tapes in wearable electronics, limiting biocompatibility when used on the human body [2,3]. Therefore, we are trying to develop a hydrogel-based touch panel that is biocompatible, self-healing, environmentally compatible (especially for temperature), and strongly adhesive in the air and underwater. Moreover, many natural organisms (such as tree frogs, red flat bark beetles, *etc.*) can survive in extremely cold environments by preventing ice crystal formation in their cells [39]. These organisms accumulate cryoprotectants like urea and glucose, lowering the freezing point of their body fluids [48]. Inspired by this, different cryoprotectants could be used to prepare anti-freezing hydrogels [27,44,46–51]. Glycerin, as widely used cryoprotectant, is a polyol with properties like a high boiling point, low volatility, and good water solubility. It offers advantages such as anti-freezing, low toxicity, and high plasticity. Glycerin molecules can form clusters with water molecules in the hydrogel matrix, breaking hydrogen bond networks and preventing ice crystal formation (*e.g.*, freezing at low temperatures) and water evaporation (*e.g.*, dehydration at high temperatures or for extended periods). Glycerol also can lower the freezing point of the organic hydrogel and enhance the resistance ability to dehydration by reducing saturated vapor pressure [43]. In addition, inspired by nature's adhesive strategies in organisms like mussels and gooseberries [52,53], a combinatorial strategy of catechol chemistry and electrostatic kinetics could be used to synthesize the underwater adhesives. Catechol-containing hydrogels have been extensively studied but often exhibit weak underwater adhesion when the catechol group acts alone. However, strong electrostatic complexation in the gel and abundant catechol groups on the TA surface can jointly promote durable underwater adhesion [45,54]. Up to now, some key challenges like weak underwater adhesion and complex preparation processes still hinder their application in wearable flexible electronics.

In this study, we designed and prepared a biomimic organic hydrogel with self-adhesion, self-healing, anti-freezing, anti-drying and conductive abilities composed of tannic acid (TA), acrylic acid (AA), acrylic acid *n*-hydroxysuccinimide ester (AA-NHS), glycerol, aluminum chloride (AlCl₃), photo-crosslinker gelatin methacryloyl (GelMA), and UV initiator α -ketoglutaric acid (AKG) and gelatin. The resulting gelatin-PAA-based organic

hydrogel (PC-OH) exhibits remarkable properties, including biocompatibility, high transparency (87 % visible light transmittance), self-adhesion to the skin in air (approximately 967 J/m²) or underwater (approximately 428 J/m²) conditions, anti-freezing capabilities (down to -60 °C), anti-drying capabilities (up to 60 °C), rapid self-healing (within 4 seconds in air or underwater), long-term stability (up to 7 days) over a wide temperature range (-20 ~ 60 °C), high stretchability (up to ~1700 % at 60 °C and ~1200 % at -20 °C), and conductivity across a broad temperature range (ionic conductivity of 1.93 S m⁻¹ at 60 °C and 3.13×10^{-3} S m⁻¹ at -30 °C). Basing on these features of PC-OH hydrogel, we constructed a surface capacitive touch system to demonstrate its practical application. This touch-sensing panel possesses high stretchability, transparent, anti-freezing, anti-dehydration, self-healable, and self-adhesive human-machine interface capacities, which can be integrated with the skin under abnormal temperature and humidity conditions. The great potential of the hydrogel in the touch panel was validated through tasks such as writing text, drawing figures, and playing electronic games, showcasing its potential in various fields that require reliable electromechanical performance.

Results

Preparation of PC-OH Organic Hydrogel

The preparation of the gelatin-PAA-based organic hydrogel (PC-OH) involves three main steps, as shown in [Figure 1A](#). First, the precursor solution was prepared by dissolving acrylic acid (AA), gelatin, tannic acid (TA), acrylic acid *n*-hydroxysuccinimide ester (AA-NHS), aluminum chloride (AlCl₃), photo-crosslinker gelatin methacryloyl (GelMA), and UV initiator α -ketoglutaric acid (AKG) in Milli-Q water. Next, the gelatin-PAA-based hydrogel (PC-H) was obtained through UV curing of the precursor solution. Finally, the gelatin-PAA-based organic hydrogel (PC-OH) was created by immersing the resulting PC-H in a water/glycerol binary solvent (1: 1, v/v) for 4 hours. During this soaking process, glycerol molecules partially replace water molecules in the PC-H hydrogel. Simultaneously, a multitude of hydrogen bonds were formed between the gelatin and glycerol, resulting in the transformation of organic hydrogel with excellent anti-freezing and anti-drying properties.

Various compounds are involved in the PC-OH organic hydrogel network to perform specific functions (Figure 1B). In the network, gelatin, and PAA create a double network structure. The physically cross-linked gelatin network acts as a sacrificial bond during deformation, enhancing the hydrogel's recovery ability and enabling dynamic energy dissipation. The chemically cross-linked PAA network enhances the mechanical strength of the organic hydrogel. Various interactions, including hydrogen bonds, covalent bonds, and electrostatic interactions, are integrated into the network to improve hydrogel adhesion in water and air. The organic hydrogel surface exhibits high adhesion in air and water due to the presence of tannic acid (TA), which contains a substantial number of catechol and pyrogallol groups, and AA-NHS esters with positively charged primary amine groups. TA, a biocompatible polyphenolic compound, is widely employed as a self-adhesive monomer with excellent adhesion properties due to its high content of catechol and pyrogallol groups (25 hydroxyl and 10 carbonyl groups). Consequently, TA can form hydrogen bonds with Gelatin-PAA chains. The free catechol/pyrogallol groups in TA enable the organic hydrogel to form hydrogen bonds, ionic coordination, and Michael additions at the matrix interface, thereby improving the interfacial bonding at the organic hydrogel-tissue interface. The AA-NHS ester group can establish covalent amide bonds with the skin, promoting rapid and robust adhesion at the organic hydrogel-tissue interface through amide covalent cross-linking. To optimize the performance of the organic hydrogels, AlCl_3 was added to achieve excellent electrical conductivity and sensing properties. This was achieved through the free movement of aluminum (Al^{3+}) and chloride (Cl^-) ions and the formation of metal ion coordination interactions with free carboxyl groups on PAA chains and phenolic hydroxyl groups on TA in the cross-linked network, which enhanced the mechanical strength of the organic hydrogels and met the requirements of ion electronic devices.

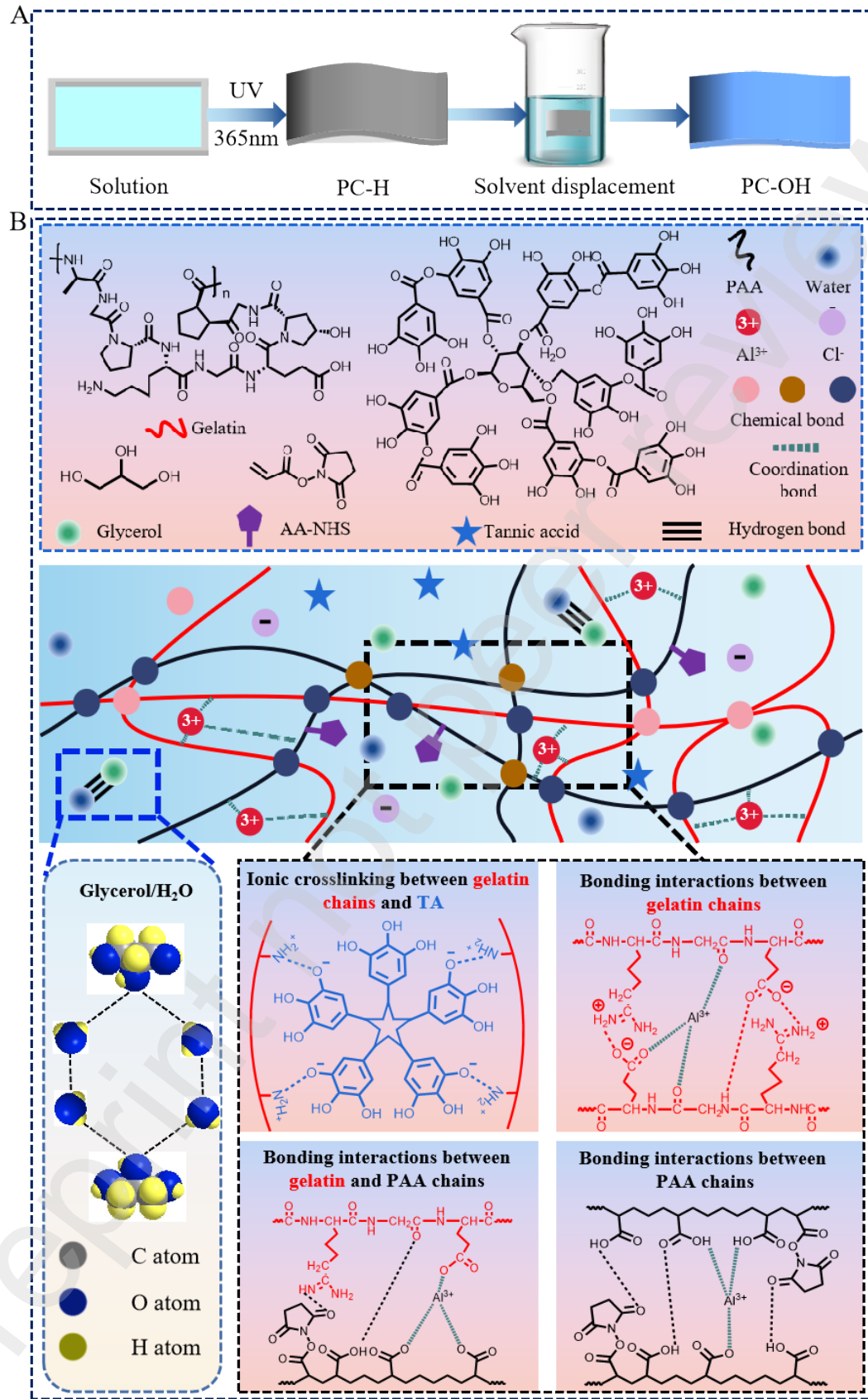


Figure 1: Schematic diagram of PC-OH organic hydrogel preparation. (A) The synthesis process of PC-OH is depicted in this schematic. (B) This diagram illustrates the physicochemical network structure and mechanism of PC-OH.

To ensure the organic hydrogel's mechanical stability in diverse environments, we introduced a glycerol-water binary solvent system. This system effectively lowers the network's freezing point, preventing water evaporation and ice crystal formation below zero degrees (Figure 1B). Moreover, due to the formation of numerous hydrogen bonds between water and glycerol, PC-OH organic hydrogel exhibits excellent water retention properties. Consequently, the PC-OH organic hydrogels synthesized in this work are suitable for prolonged practical applications.

We characterized the morphology of PC-H and PC-OH samples using scanning electron microscopy (SEM). The PC-H hydrogel surface exhibits a relatively sparse structure with pores of varying sizes (Figure 2A.). This unique porous architecture facilitates the movement of conducting ions, contributing to its high electrical conductivity. Conversely, Figure 2B illustrates that PAA-OH has a smooth and flat morphology due to increased cross-link density attributed to glycerol. Fourier-transform infrared spectroscopy (FTIR) (Figure 2C) was employed to confirm the interaction network of the PC-OH organic hydrogel. Significant absorption bands were observed at approximately 1635 and 1230 cm⁻¹, corresponding to the carboxyl group C=O stretching vibration and the NHS ester C-N-C stretching vibration, respectively. These bands indicate the successful grafting of the NHS ester onto the gel network polymer chain. Additionally, characteristic peaks corresponding to O-H stretching vibrations appeared for both PC-H and PC-OH at approximately 3340 cm⁻¹. In the presence of glycerol, the PAA-OH absorption band was more pronounced than that of PC-H, indicating enhanced OH stretching vibrations. Wearable sensor devices require the ability to assess skin conditions. Ionic conductive hydrogels offer an effective means of producing transparent and highly resilient hydrogels. Both PC-H hydrogels and PC-OH organic hydrogels were found to be transparent through ultraviolet-visible-near infrared spectrophotometry (UV-Vis-NIR) analysis in the visible band of 400 ~ 800 nm. However, PC-OH organic

hydrogels exhibit even greater transparency, with light transmission exceeding 87% ([Figure 2D](#) and [E](#)). This exceptional transparency makes PC-OH organic hydrogel highly promising for applications in the field of wearable sensors for visual interaction. Ideal wearable touch panels need to be non-toxic and biocompatible.

To quantitatively assess the biocompatibility of PC-OH, we conducted fluorescence imaging and the MTT assay to evaluate the in vitro cell viability of PC-OH extracts ([Figure S1](#), Supporting Information)^[25]. Confocal laser scanning microscopy (CLSM) was employed to observe live cells. The CLSM images revealed no significant decrease in cell viability in the PC-OH extract hydrogel medium culture compared to the control group. To further assess cell proliferation, growth curves of A549 cells were generated ([Figure 2F](#)). These curves depicted the proliferation levels of cells subjected to different treatments of PC-H and PC-OH at various time points (24h, 48h, and 72h). The cell viability was determined using the CCK-8 assay. The viability of A549 cells treated with PC-OH showed no significant difference from that of the control group. After 72 hours of incubation, the absorbance of the control and PC-OH-treated A549 cells at 540 nm was 3.41 and 3.24, respectively, with a difference of less than 5%. These results strongly suggest that PC-OH exhibits excellent biocompatibility and holds promise for applications in biocompatible wearable electronic devices.

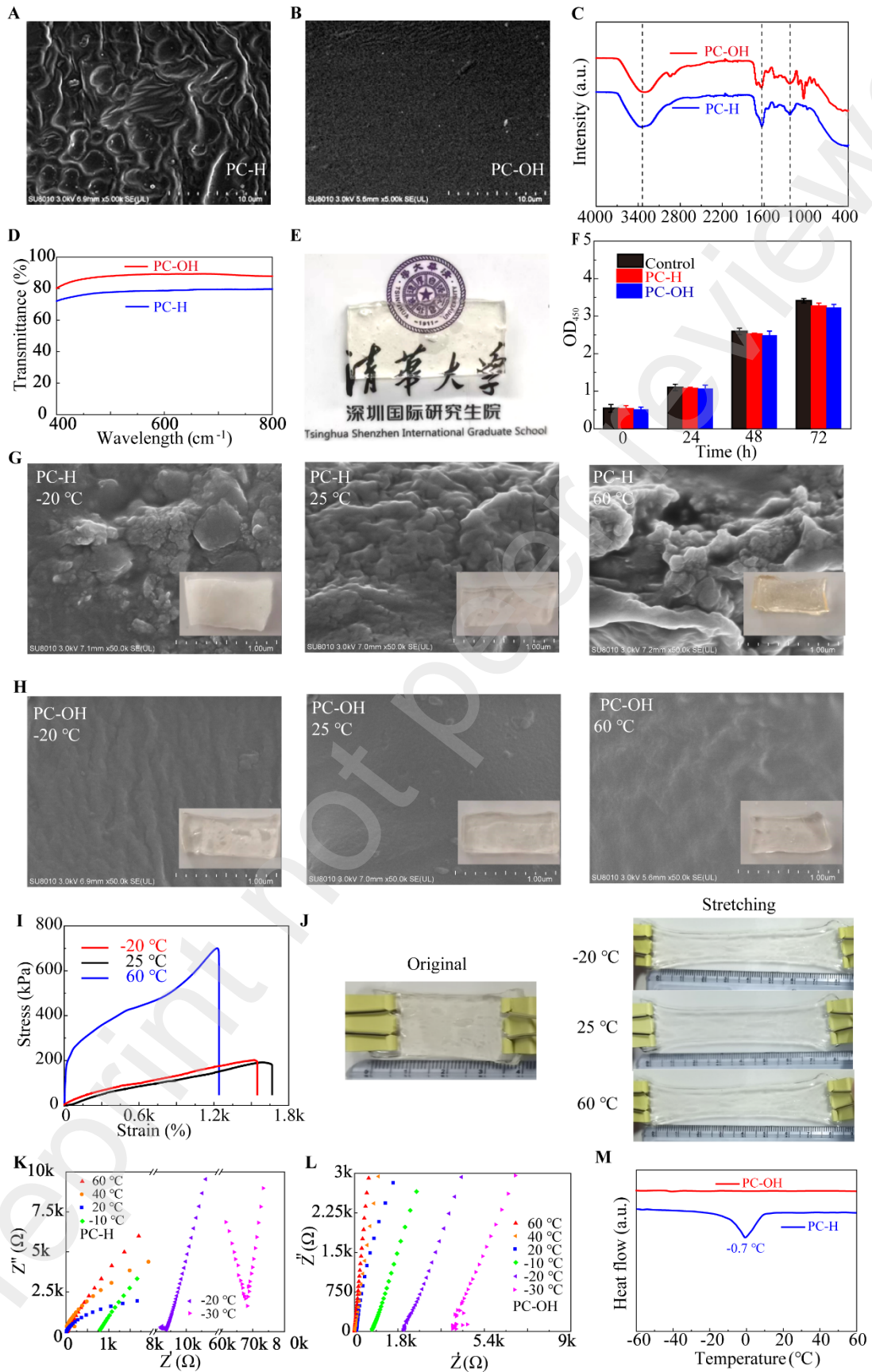


Figure 2. Physical properties and biocompatibility of PC-OH organic hydrogels. SEM pictures of PC-H (A) and PC-OH (B). ATR-FTIR of PC-H and PC-OH (C). Transmission spectra of 2.0-mm thick PC-H and PC-OH films (D). Photographs of logo and text covered by 2.0-mm thick PC-OH films (E). Cell proliferation was assessed by the CCK-8 assay of PC-H and PC-OH after 24h, 48h, and 72h of A549 cells incubation, Control: Deionized water (Milli-Q, $18.2\text{ M}\Omega\text{ cm}^{-1}$) (F). SEM images of PC-H at -20, 25, and 60 °C (G) and PC-OH at -20, 25, and 60 °C (H). Inset: digital photos of PC-H and PC-OH at -20, 25, and 60 °C. Stress-strain curves of PC-OH at different temperatures (-20, 25, and 60 °C) (I). Digital photos of original PC-OH and tensile performance at -20, 25, and 60 °C (J). Demonstration of the electrical property of PC-OH: Nyquist plots of PC-H (K) and PC-OH (L) at determined temperatures from -20 ~ 60 °C. DSC curves of PC-H and PC-OH (M).

Anti-Freezing and Anti-Dehydration Properties of PC-OH

In hydrogel-based electronics, temperature sensitivity presents a significant challenge, as these materials can freeze at sub-zero temperatures and dehydrate at elevated temperatures, resulting in the loss of essential properties. To address this issue, we selected glycerol as a hygroscopic and anti-freezing agent due to its low biotoxicity when in contact with skin and its neutral charge, which minimizes adverse effects on the ionic crosslinking network and charged groups within the adhesive layer. Glycerol's presence enhances anti-freezing and anti-dehydration properties in organic hydrogels by disrupting hydrogen bonds between water molecules while forming strong hydrogen bonds with water^[42,49]. The integration of glycerol into organic hydrogels ensures their adaptability to different temperatures while maintaining excellent mechanical and electrical conductivity.

We conducted SEM characterization to assess the ability of PC-OH to withstand extreme temperatures. Figure 2G and H demonstrate that the microstructure of PC-H is compromised at both -20°C and 60°C. In contrast, PC-OH exhibits no significant structural changes, indicating that its microstructure remains intact even under extreme temperature conditions. This resilience is attributed to the abundance of hydrogen bonds formed between water and glycerol within the organic hydrogel network, which inhibits

ice crystal formation and water evaporation. Optical photographs (Inset in Fig. 2G and H) reveal that at -20°C, PC-H hydrogel becomes stiff and brittle due to complete freezing, while PC-OH remains highly flexible and can endure strains of up to \approx 1500% (Figure 2I and J; and Figure S2 and S3, Supporting Information). At 60°C, PC-H hydrogel loses elasticity and functionality due to water loss, whereas PC-OH maintains excellent tensile properties and can withstand strains of \approx 1200% due to the presence of glycerol solvent. The numerous hydrogen bonds between water and glycerol molecules effectively impede water loss, thus preserving the gel's stable mechanical properties. Interestingly, the fracture tensile strength of PC-OH organic hydrogels significantly increases at higher temperatures (60°C) compared to lower temperatures (-20°C) and room temperature (25°C). This phenomenon is attributed to increased water loss at higher temperatures, which further strengthens hydrogen bonds between polymer chains, resulting in improved mechanical properties such as Young's modulus and fracture stress^[40]. Maintaining stable conductivity across a broad temperature range, from -20°C to 60°C, is crucial for hydrogel-based electronic devices. Figure 2K and L present Nyquist plots of PC-OH organic hydrogels and PC-H hydrogels, revealing that the conductivity of PC-OH organic hydrogel is less affected by temperature variations compared to PC-H hydrogel. The electrical conductivity (σ) was calculated from the plots using the formula $\sigma = d/RS$, where d represents the thickness of the gels, S denotes the gel's surface area, and R is the point value intersecting the Z' axis. The conductivity of PC-OH organic hydrogel decreases only moderately with temperature changes at 60°C and -30°C, with values of 1.93 S m⁻¹ and 3.13×10^{-3} S m⁻¹, respectively (Figure S, Supporting Information). In contrast, PC-H hydrogel exhibits a substantial decrease in conductivity at lower temperatures, registering 1.38 S m⁻¹ at 60°C and 1.87×10^{-4} S m⁻¹ at -30°C. These changes in conductivity are attributed to the freezing and dehydration of hydrogels at extreme temperatures. Water crystallization within the hydrogel network at freezing temperatures hinders ion movement, leading to a decline in ionic conductivity. Conversely, gel dehydration at high temperatures results in water evaporation, followed by reducing the solubility of AlCl₃ in the solvent and causing a decline in ionic conductivity. However, PC-OH's conductivity remains relatively stable across different temperatures (-20 °C to 60 °C) (Figure 2K and L). This can be attributed to the hydrogel's

environmental adaptability, with numerous hydrogen bonds forming between water and glycerol molecules. To further validate the anti-freezing properties of PC-OH organic hydrogels, we conducted a differential scanning calorimetry (DSC) analysis. Remarkably, the DSC curve of PC-OH displayed no crystallization peak across a wide temperature range from -60°C to 60°C (Figure 2M), indicating the absence of ice crystal formation. Unlike conventional hydrogels that typically freeze at sub-zero temperatures due to their high water content, PC-OH, thanks to the addition of glycerol, remains free from ice crystal formation.

Long-Term Stability of PC-OH Organic Hydrogel

The prolonged use of soft materials like hydrogels in practical applications poses a significant challenge due to the potential for dehydration over time. Moisture loss can lead to structural and functional failures, limiting the viability of hydrogels in long-term wearable electronics^[42,43,47]. To assess the mechanical stability of PC-H and PC-OH, we subjected samples of PC-H and PC-OH (dimensions: 20.0 × 10.0 × 2.0 mm³) to room temperature conditions (25°C, 38% RH) for 7 days while applying various mechanical stresses such as stretching, bending, and twisting. PC-H lost its elasticity and stretchability due to water loss, while PC-OH retained its ability to be reversibly stretched, bent, and twisted (Figure 3A). Additionally, tensile tests were conducted to evaluate the mechanical properties of PC-OH after 7 days of room temperature storage (25 °C, 38% RH) compared to its original condition (Figure 3B). The results revealed a significant decrease in the failure strain of PC-H (<10%) after 7 days, compared to the initial condition (\approx 1600 %). Conversely, even after 7 days, PC-OH maintained the ability to endure strains of over 600 %. Furthermore, Young's modulus of PC-H increased considerably over time, ranging from 0.32 to 283.75 MPa, while PC-OH exhibited a relatively stable Young's modulus (0.72 to 3.65 MPa) (Figure 3C). These notable changes in PC-H's mechanical parameters resulted from substantial water loss within the hydrogel network. In contrast, PC-OH, bolstered by glycerol's presence, exhibited improved water retention through hydrogen bonding with water molecules, mitigating water evaporation. We also examined changes in the mass and conductivity of PC-H and PC-OH samples after 7 days of room temperature storage, shedding light on the environmental stability of

PC-OH under prolonged use. We observed a slight initial increase in PC-OH's mass, followed by a decrease over time, reaching 90% of its initial state by the seventh day ([Figure 3D](#)). This phenomenon can be attributed to the numerous hydroxyl groups within glycerol molecules, which result in lower water vapor pressure within the PC-OH gel matrix compared to the external environment. Conversely, the mass of PC-H hydrogels consistently and rapidly decreased to 20% of their original mass after 7 days at room temperature. This substantial mass reduction stemmed from the original hydrogel matrix lacking glycerol, resulting in higher internal water vapor pressure than in the surrounding environment. PC-H hydrogel's conductivity showed a decreasing trend (approximately 0.001 S m^{-1} after 7 days of storage) due to gradual water molecule evaporation within its network, which limited ion mobility ([Figure 3E](#)). In contrast, PC-OH experienced only minor conductivity decreases due to increased water evaporation, which raised the concentration of polymer chains and reduced ion mobility, during 7 days of storage at high humidity conditions (RH = 65 %). However, the conductivity remained at $\approx 0.1 \text{ S m}^{-1}$ after 7 days, still adequate for sensing purposes. This behavior can be explained by the lower ionization constant of glycerol compared to water, facilitating solvent molecule dissociation and generating more free-flowing ions (*i.e.*, H⁺). Additionally, glycerol's inclusion improved water retention within the organic hydrogels, as the abundant hydroxyl groups facilitated strong hydrogen bonds with water molecules, reducing water loss and maintaining ionic conductivity relatively high over 7 days (100 times higher than PC-H after 7 days of storage). Furthermore, AlCl₃ played a crucial role in enhancing the ionic conductivity of PC-OH organic hydrogels by dissolving in water and interacting with carboxylate ions and phenolic hydroxyl groups within the organic hydrogel network. Through this interaction and by dissolving within the organic hydrogel network, AlCl₃ effectively improved the conductivity of the organic hydrogels, as it could freely move within the network, hydrating through hydrogen bonds with water molecules.

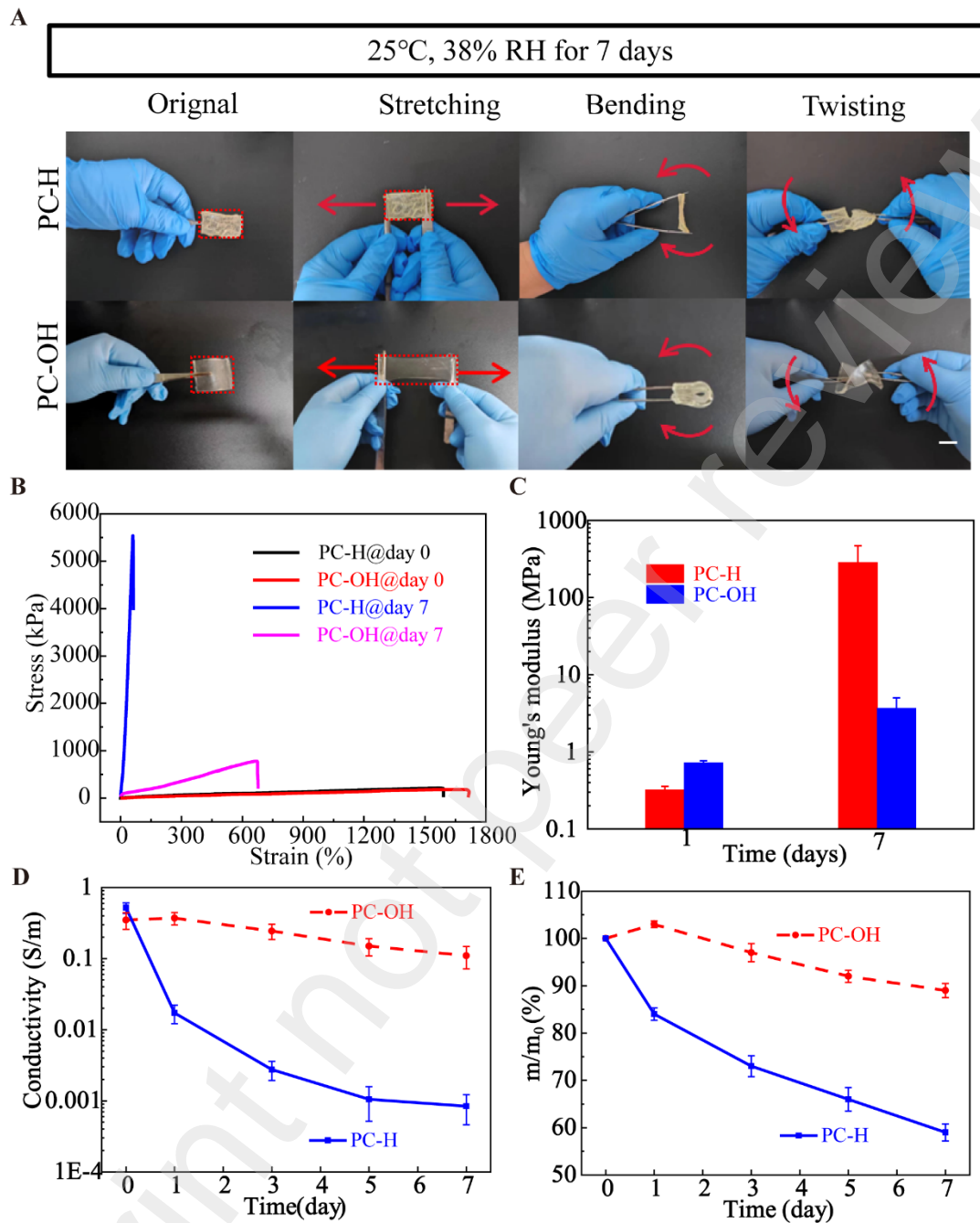


Figure 3. Environmental stability of PC-OH. Photographs of PC-H and PC-OH in tension, bending, and twisting after 7 days of storage at room temperature (A). Photographs of PC-H and PC-OH at room temperature for 7 days (B). Photographs of PC-H and PC-OH at room temperature for 7 days (C). Variation of mass of PC-H and PC-OH at room temperature for 7 days with time (D). Variation of conductivity of PC-H and PC-OH with time at room temperature for 7 days (E).

Electromechanical Self-Healing Properties of PC-OH

Wearable and stretchable ionic electronics often endure repetitive stresses and external forces that can lead to mechanical damage, such as abrasions, scratches, and cuts, ultimately shortening their lifespan. Integrating organic hydrogels with self-healing abilities can enhance the lifetime of ionic electronic devices. The PC-OH organo-hydrogels featured in this study demonstrate autonomous electromechanical self-healing capabilities, as exemplified by their ability to repair visible cuts in the material. To illustrate this, we initially cut a sample into two separate pieces. These sections were then gently reconnected, allowing polymer chains within the hydrogel to diffuse into the interface over time. This created a topological entanglement with the other part of the network, enabling the hydrogel to heal without the need for additional materials. Remarkably, without any external stimulation, the separated pieces of PC-OH exhibited impressive mechanical self-healing properties upon contact. [Figure 4A](#) shows an optical microscope image of the organic hydrogel sample's self-healing process when left at room temperature for 24 hours, revealing that the cut interface disappeared after this period ([Movie S1](#), Supporting Information). In this study, we define the ratio of recovered strain to the original strain as mechanical self-healing efficiency. All cut and self-healed PC-OH organic hydrogels maintained a consistent Young's modulus and exhibited a uniform tensile stress distribution at different temperatures (-20 ~ 60°C) even when submerged in water. Mechanical properties of PC-OH were self-recovered at all temperatures, including as low as -20°C. In [Figure 4B](#), the mechanical self-healing efficiencies were 87.58%, 90.8%, and 92.3% after 24 hours of self-healing at different temperatures (-20, 25, and 60°C). Notably, the mechanical self-healing efficiency of PC-OH increased with higher temperatures and longer self-healing times, indicating that the thermal movement of the polymer accelerated and promoted the formation of new cross-linking sites. Impressively, PC-OH organic hydrogel also demonstrated strong underwater self-healing ability. In [Figure 4C](#), after 24 hours of self-healing in water at 25°C, the tensile stress and strain of the healed PC-OH organic hydrogel were ≈0.12 MPa and ≈1100%, respectively, relative to the pristine sample immersed in water, resulting in a mechanical self-healing efficiency of more than 88% for PC-OH. Besides mechanical

self-healing, the electrical self-healing ability of hydrogels is crucial for the durability of ionic electronic devices. In this work, the ionic conductivity of PC-OH organic hydrogels also exhibited self-healing properties. [Figure 4D](#) and [E](#) illustrate a photograph of a PC-OH organic hydrogel strip connected in series with a red light-emitting diode (LED) at room temperature. We initially cut the strip into two parts, immediately reconnected them, and illuminated the red LED. After gentle stretching, mechanical self-healing of the PC-OH organic hydrogel was observed, and the red LED remained illuminated even in the stretched state, confirming the reliable electromechanical self-healing abilities of PC-OH. Real-time electrical self-healing of PC-OH organic hydrogel is demonstrated in [Figure 4F](#). Initially, the current in the PC-OH organo-hydrogel strip remained stable. When we quickly cut the strip into two parts with a sharp ceramic knife, a sharp decrease in current immediately occurred, indicating discontinuity in the ion transport pathway in the separated part. After complete separation, the current dropped to zero. However, reconnecting the two separated parts, we observed that within just 4 seconds, the current had recovered to 87% of the initial current, demonstrating that the organic hydrogel is electrically self-healing when the ion transport channel is reconstructed. Furthermore, the current in the cut-reconnected PC-OH gradually recovered within 24 hours after self-healing at -20°C, 25°C, and 60°C, corresponding to electrical self-healing efficiencies of 89%, 94%, and 98%, respectively. PC-OH exhibited an electrical self-healing efficiency exceeding 92% after 24 hours of self-healing in water at 25°C ([Figure 4G](#)). These results indicate that PC-OH autonomously possesses electrical self-healing capabilities even after being damaged over a wide temperature range, both in air (-20 ~ 60°C) and underwater.

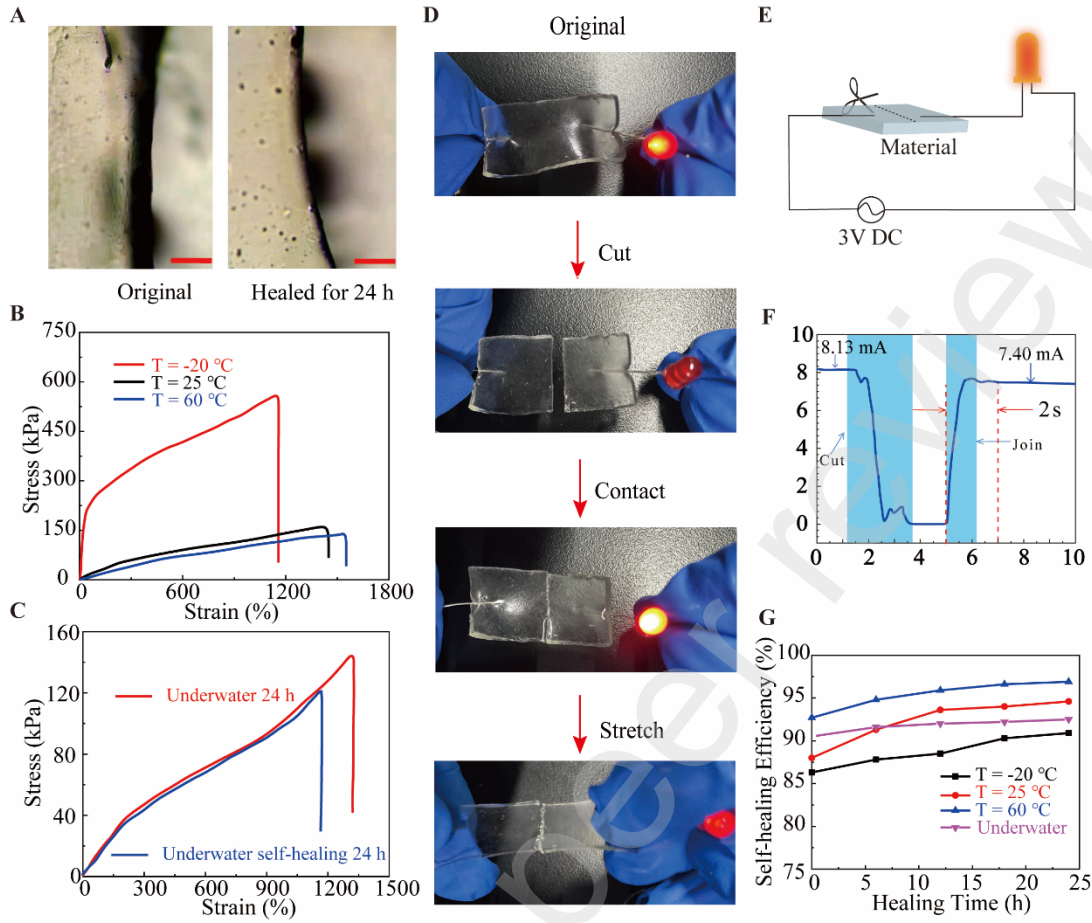


Figure 4. Electromechanical self-healing performance of PC-OH. Optical microscope images of the PC-OH organic hydrogel autonomous self-healing process at 25 °C (A). After self-healing at -20, 25, and 60 °C with 24 h (B), the stress-strain curves of PC-OH specimens. After 24 h storage and self-healing underwater at 25 °C (C), the stress-strain curves of PC-OH specimens. The self-healing process using red LED demonstrates PC-OH's conductivity (D, E). Current flowing through PC-OH Vs. Time of PC-OH organic hydrogel in its original state, cut and reconnected at 25°C (F). Electrical self-healing efficiency Vs. Self-healing time after 24 hours of storage in different environments (-20, 25, 60°C and underwater) (G).

Adhesion Property of PC-OH in Air and Underwater

In hydrogel-based flexible wearable ionic electronics, the adhesive ability of hydrogels plays a pivotal role in ensuring reliable functionality. It guarantees a consistent and stable connection between the electrodes of the electronics and the underlying substrate,

reducing the need for external auxiliary tapes with high interfacial resistance and mitigating motion artifacts caused by these tapes^[41]. The PC-OH network leverages multiple interactions, including hydrogen bonding and various electrostatic interactions, to excel in adhesion. These interactions occur between amino groups in tissues and functional groups within the organic hydrogel, such as the dynamic catechol chemistry of TA, carboxyl groups of PAA, and hydroxyl groups in the solvent system^[52]. Moreover, covalent interactions, such as amide bonding, take place between active-NHS groups and tissue amino groups at the hydrogel-tissue interface, contributing to robust adhesion on human skin.

As depicted in [Fig 5A](#), PC-OH organic hydrogels exhibit strong adhesion to various substrates, whether inorganic or organic, including plastic (PE), paper (cellulose), glass, stone, steel, and rubber. This versatility makes PC-OH organic hydrogels suitable for a wide range of applications. To quantitatively assess adhesion strength, a lap shear test was conducted by sandwiching a hydrogel assembly between substrate pairs. The maximum adhesion strength, measured at the point of interfacial disruption, was determined. The results reveal adhesive strengths of 11.5 kPa, 9.2 kPa, and 5.1 kPa for the stone/skin, paper/skin, and glass/skin interfaces, respectively ([Figure 5B](#) and [C](#)). Notably, the high adhesive strength of stone and paper substrates can be attributed to their rough surfaces, which increase the contact area with PC-OH organic hydrogel. These findings demonstrate that PC-OH organic hydrogel excels in shear tests, dissipating energy during the peeling process, thereby maintaining a significant peeling force. PC-OH organic hydrogels exhibit strong adhesion to metals, even in the presence of excess water, as illustrated in [Figure 5D](#). The adhesion capability extends to human skin both in the air and underwater ([Figure 5E](#) and [F](#)). PC-OH adheres firmly to the human forearm, conforming to the skin when peeled. It can then be pulled up in both air and underwater conditions, underscoring PC-OH's excellent adhesion properties. To quantitatively characterize underwater adhesion, a lap shear test was performed to measure the interfacial adhesion between PC-OH and skin under normal and humid conditions. Porcine skin, resembling human skin, was used for testing. In the air, the interfacial adhesion energy between PC-OH and porcine skin measured $\approx 967 \text{ J}\cdot\text{m}^{-2}$ ([Figure 5G](#) and [H](#)), enabling stable adhesion for wearable sensing applications. During

water immersion, the adhesion energy tends to decrease due to the inhibitory effects of water on interfacial interactions and the hindrance of conformal contact at the interface. It is worth noting that the robust adhesion of PC-OH organic hydrogels to different surfaces, whether rigid metal electrodes or flexible polymer substrates, benefits soft electronic systems that often encounter exposure to liquids like sweat and rain. The exceptional adhesion of PC-OH organic hydrogels can be attributed to a synergistic effect of chemical interactions and energy dissipation during the peeling process (Figure 5I). Abundant functional groups in PC-OH organic hydrogels, particularly phenolic hydroxyl groups in TA and -NHS groups in AA-NHS ester, foster various non-covalent interactions like ion-dipole, metal coordination bonds, and hydrogen bonds with substrates [41]. Additionally, dynamic metal coordination bonds and hydrogen bonds in PC-OH organic hydrogels provide dissipation mechanisms at the interface, requiring additional energy for interfacial crack expansion. These results underscore the potential of PC-OH organic hydrogels for use in soft electronic systems, especially in humid conditions.

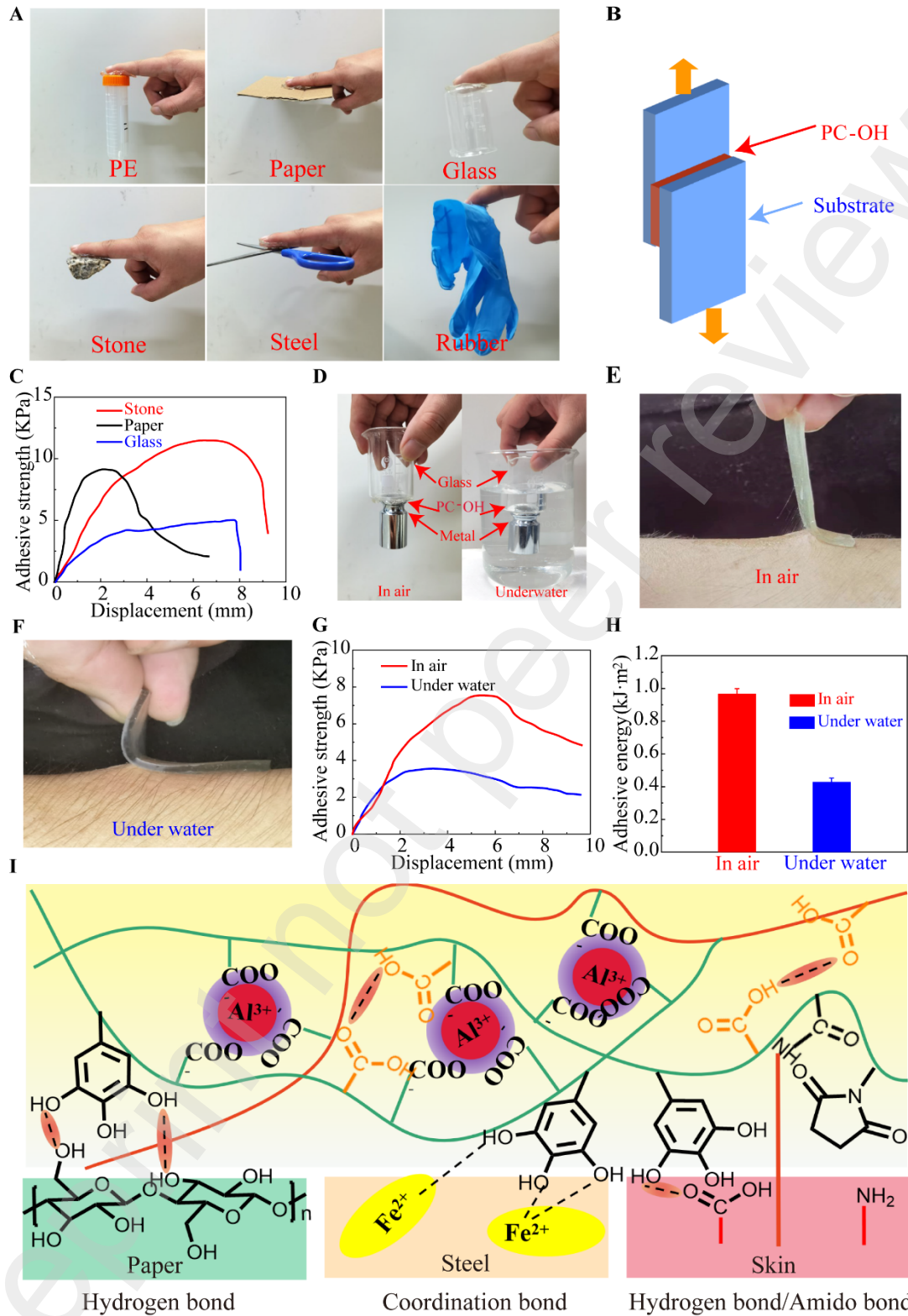


Figure 5. Adhesive behaviors of the PC-OH organic hydrogel. Hydrogels can adhere to various substrate surfaces (plastic (pe), paper (cellulose), glass, stone, steel, and rubber)

(A). Schematic illustration diagram of the lap shear test (B). The adhesive strength curves of lap shear tests on stone, paper (cellulose), glass, and porcine skin glued by the PC-OH hydrogel (C). PC-OH organic hydrogel adhered to glass and metal and sustained adhesion in air and underwater (D). Photographs of PC-OH adhered to human skin in the air (E) and underwater (F). Adhesive strength (G) and adhesive energy (H) of PC-OH organic hydrogel adhered to pig skin in the air and underwater. Adhesion mechanism between the PC-OH and various substrates (wood (cellulose), metal (steel), and human skin) (I).

PC-OH Touch Strip

In our quest to evaluate the potential of PC-OH in e-skin applications, we conducted experiments utilizing both 1D and 2D touch sensors. For our 1D configuration ([Figure 6A](#)), we applied in-phase alternating current to both ends of the PC-OH touch strip using A1 and A2 current meters, which were connected to copper (Cu) electrodes. When a human finger makes contact with the 1D strip, a coupling capacitance (C_{finger}) forms at the finger/PC-OH interface, creating a closed-loop circuit through which current flows into the human body and subsequently to the ground. To understand this system better, we examined the equivalent circuit of the PC-OH 1D touch strip ([Figure 6C](#)). This circuit divides the strip into two resistive segments upon contact with a finger. Additionally, we explored the touch strip's position-sensing capabilities ([Figure 6C-E](#)). Here, we observed that the current flowing through the circuit varied with the point of contact. This variation in current magnitude depended on the parasitic capacitance, which generated the baseline current, and the additional current produced by finger touch. The baseline current, stemming from leakage to the environment through the PC-OH touch panel, serves as a reference point. Notably, when the PC-OH touch strip came into contact with a finger, it generated additional current as it flowed from the electrode to the grounded finger. This phenomenon is visually represented in [Figure 6D](#) and [E](#). Moreover, the PC-OH strip was touched point by point with a finger, moving from left to right (from $\alpha = 0.0$ to 1.0) with α incrementing in steps of 0.2 ([Figure 6E](#)). We measured the current using A1 and A2 current meters. We observed that the total current, denoted as I_t , remained constant as the touch position changed from $\alpha = 0.0$ to 1.0. Additionally, the decrease in the peak current

for I_1 exhibited near-linear behavior, while the increase in the peak current of I_2 also followed a nearly linear pattern. These results confirm that the touch current induced by finger contact is directly proportional to the distance between the electrode and the touch point, thus demonstrating the 1D PC-OH touch strip's position-sensing ability. Impressively, this touch strip exhibited stable performance across a wide temperature range (-20 ~ 60°C). [Figure 6F-H](#) present how temperature variations influenced the current in the PC-OH touch strip. The baseline currents were measured at 3.83 μ A, 4.34 μ A, and 5.13 μ A at -20, 25, and 60°C, respectively. The conductivity of PC-OH increased with rising temperature, leading to a higher baseline current. Concurrently, finger touch-induced additional current exhibited significant changes with temperature. For instance, at $\alpha = 0.2$, the additional touch currents for I_{11} measured 0.69 μ A, 0.99 μ A, and 1.31 μ A at -20, 25, and 60°C. Furthermore, we investigated to assess the effect of strain on the sensing capabilities of the PC-OH touch strip. To do this, we stretched the 2D strip to double its initial length ([Figure 6I](#)). We subsequently touched it from the left ($\alpha = 0.0$) to the right ($\alpha = 1.0$) in steps of $\alpha = 0.2$, point by point. During this process, it was observed that in the stretched state, the parasitic capacitance of the PC-OH touch strip increased due to the expanded contact area with the environment. Consequently, both baseline current and additional touch current increased in tandem after stretching compared to the initial state. Specifically, with the strip stretched, the baseline current increased from 4.34 μ A to 7.36 μ A. Importantly, when a finger made contact with the stretched strip, the induced current was added to the baseline current. Notably, the touch current of the strip in the stretched state measured 0.96 μ A when touched with a finger at position $\alpha = 0.2$, which was similar to the touch current in the undeformed state, measuring 0.99 μ A (currents were measured with the A1 current meter). This demonstrates that stretching did not impact the current response of the touch strip. We also investigated the impact of wet environments, including wetness, dampness, and recovery, on the sensing response of the PC-OH touch strip ([Figure 6J-P](#)). The baseline currents for the electrode were 4.46 μ A, 4.39 μ A, and 4.35 μ A, respectively. Notably, the baseline current increased significantly with rising humidity levels due to the expanded contact area with moisture. However, when touching the touch strip, the additional current generated by finger touch only exhibited slight increases with rising moisture

levels. This is because the conductivity of PC-OH remained essentially constant under these conditions. For example, the additional touch currents of the electrodes were 1.53 μ A, 1.14 μ A, and 1.02 μ A when touching at the $\alpha = 0.2$ position. The localization ability of the PC-OH touch strip for finger touch positions is also recoverable (Figure 6J-L). In Figure 6Q-T, two touch strips were cut (one at $\alpha = 0.25$, and the other at both $\alpha = 0.25$ and 0.75). These cut strips were reconnected and healed after 5 minutes and 24 hours. Figure 6Q and S illustrate that more significant current changes occurred near the reconnected interface due to the additional resistance. Furthermore, with increased self-healing time, electronic self-healing efficiency improved, while additional resistances decreased. Moreover, it was noted that the baseline current and additional current of the two cuts were generally higher than those of one cut after self-healing. This occurred because when the strip was cut and reconnected, the parasitic capacitance of the strip increased due to the expanded contact area with the environment. Consequently, leakage current flowed through the touch strip/environment-formed parasitic capacitance, increasing the currents. Figure 6R and T (self-healed after 24 hours) confirmed that the currents recorded after healing two cuts were also higher than those after healing one cut. This further emphasized that the strip's parasitic capacitance increased due to the increased touch strip/environment contact area. As α ranged from 0.0 to 1.0, the difference in output RMS currents of the touch strip is shown in Figure 6U-W. The additional touch current exhibited a linear negative relationship with the electrode/touch point distance. Therefore, using the RMS current to analyze the touch position can exclude the effects of strain, temperature, wetness, and damage on signal perception, indicating that the PC-OH touch strip maintains high operational stability and mechanical reliability under tensile conditions, across a wide temperature range (-20 ~ 60°C), and in wet and damaged environments.

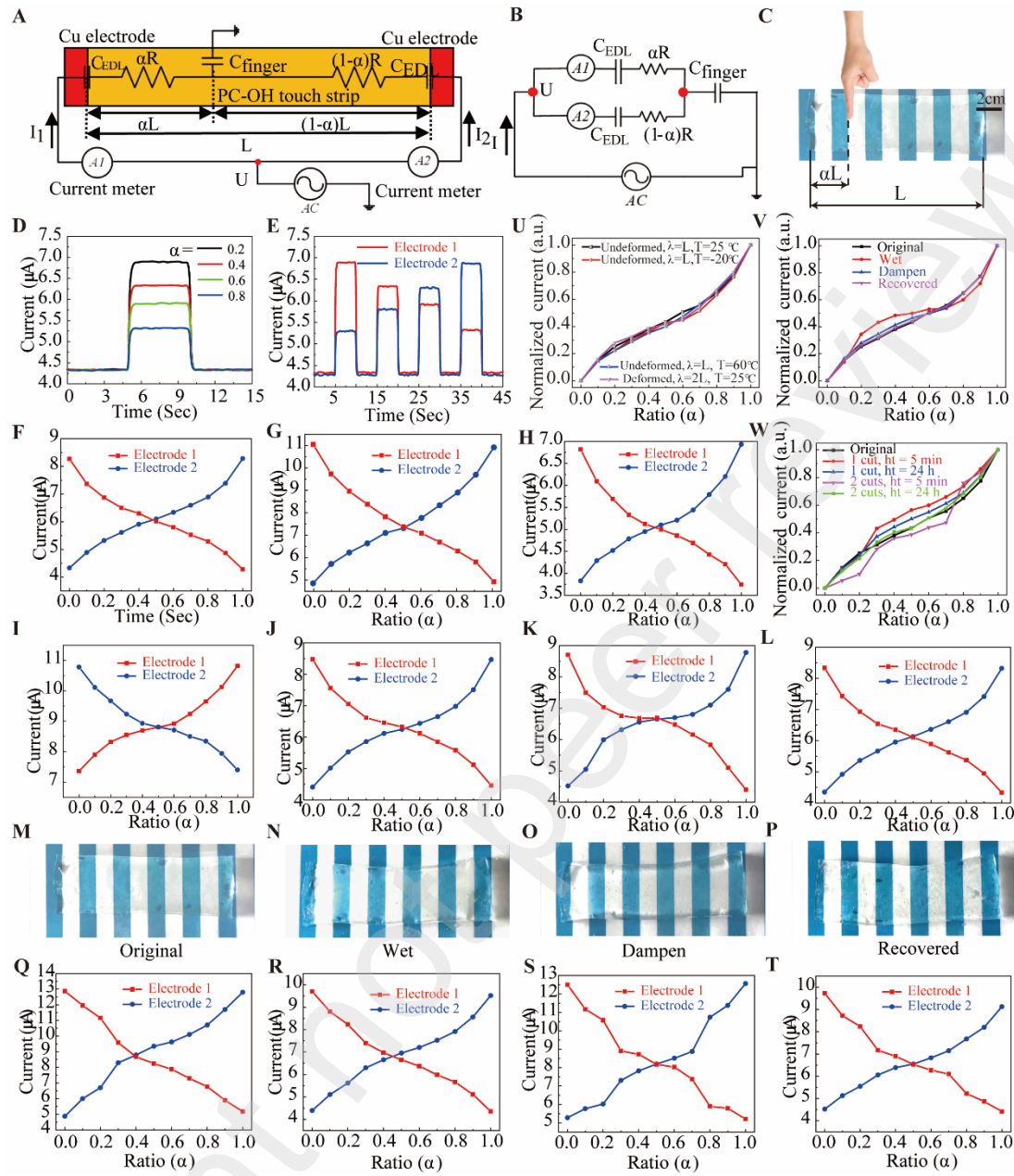


Figure 6. The operating principle of the PC-OH touch strip (A) Schematic diagram of the 1D PC-OH touch strip. A closed circuit is formed when the finger touches the strip as the finger is grounded. (B) Schematic diagram of the electrical circuit of the PC-OH strip. (C) Schematic diagram showing the definition of the electrodes and 1D strip touch position, where L is the length of the touch strip, and αL is the distance from electrode A_1 to the touch point. (D) A_1 currents for different contact points ($\alpha = 0.2, 0.4, 0.6, 0.8$). When a finger touches the strip, additional touch current flows. Therefore, the A_1 current magnitude decreases as the touch point moves far away from electrode A_1 . The current

returns to the baseline value when the strip is no longer in contact. (E) Currents measured from A1 and A2 at distances of $\alpha = 0.2, 0.4, 0.6$, and 0.8 from the contact point to the A1 electrode during the contact period. A touch strip was tested at -20°C (F), 25°C (G), 60°C (H), and in the stretched state ($\lambda = 2$) (I). A touch strip was tested at different wet environments: wet (J), dampish (K), and recovery (L), and the photos of the touch strip were tested at different wet environments: original (M), wet (N), dampish (O), and recovery (P). A strip is tested by first cutting the touch strip and then reconnecting it at $\alpha = 0.25$ and healing after 5 min (Q) and 24 h (R). A touch strip is firstly tested by cutting it and then reconnecting it at $\alpha = 0.25$ and 0.75 positions and healing after 5 min (S) and 24 h (T). The difference of the touch strip output current when α varies from 0.0 to 1.0 after stretching($\lambda=2$) at 25 , -20 , 60 , and 25°C (U). The difference of the touch strip output current when α varies from 0.0 to 1.0 at different wet environments: original, wet, dampish, and recovery (V). When the touch position α was varied from 0.0 to 1.0, the difference of the touch panel output current in the original state and after the first cut, followed by joining at only $\alpha = 0.25$ position and both $\alpha = 0.25$ and 0.75 positions, and then healed after 5 min and 24 h, respectively (W).

2D PC-OH Touch Panel and Wearable Touch Panel

Our experiment focused on a 2D PC-OH touch panel to precisely measure touchpoint positions ([Figure 7A](#) and [B](#); and [Figure S5](#) and [S6](#), Supporting Information). To set up this experiment, we connected the four corners of a 2mm thick PC-OH film to four copper electrodes. These electrodes were then linked to the same AC power source ($\pm 3\text{V}$, 17kHz) using copper wires to ensure that the voltage applied to the four corners had the same magnitude and phase. Current meters A1, A2, A3, and A4 were placed between the power source and each electrode. To describe the touchpoint on the panel, we introduced two normalized distances, α and β , as illustrated in [Figure 7A](#). The lower left corner of the touch panel corresponds to $(\alpha, \beta) = (0, 0)$, while the upper right corner corresponds to $(\alpha, \beta) = (1, 1)$. By touching various points with a finger, the touch panel was effectively divided into four virtual resistive sections. Each of these virtual resistors was linked in series with an electric double-layer capacitor (C_{EDL}) and a current meter within the circuit. These four sections were connected in parallel, and this entire configuration was

connected in series with the coupling capacitance (C_{finger}), which formed at the finger/PC-OH interface (Figure 7B). We then tested four representative touchpoints: TP#1 (0.25, 0.75), TP#2 (0.75, 0.75), TP#3 (0.75, 0.25), and TP#4 (0.25, 0.25). As the finger sequentially touched these touchpoints, the currents detected by the four current meters placed at each corner were recorded. Figure 7C-E display the recorded currents when touching the four representative touchpoints (TP#1, TP#2, TP#3, and TP#4) at different temperatures (-20, 25, and 60°C). The results indicate that the additional touch current decreases as the finger moves farther from the end of the strip. For instance, at 25°C (Figure 7C), when the finger moved from TP#1 to TP#2, the I1 current decreased from 5.25 μ A to 1.32 μ A. Subsequently, when transitioning from TP#2 to TP#3, the I1 current decreased from 1.32 μ A to 0.79 μ A. Conversely, when the touch position shifted from TP#3 to TP#4, the I1 current increased from 0.79 μ A to 1.31 μ A. Additionally, for a given touchpoint, the touch currents are inversely proportional to the corresponding distance from the finger touch point to the end of the touch strip. For example, at 25°C, the A1, A2, A3, and A4 currents at TP#1 were 11.41, 7.48, 6.76, and 7.67 μ A, respectively (Figure 7C), corresponding to additional touch currents of 5.25, 1.31, 0.97, and 1.28 μ A for I1, I2, I3, and I4, respectively. These values align with the normalized positions α and β of 0.26 and 0.74 for TP#1, respectively (Table S1, Supporting Information). As depicted in Figure 7C-E, the output positions closely match the input positions across different temperatures (-20°C, 25°C, 60°C), confirming that the 2D PC-OH touch panel effectively detects finger contact positions over a broad temperature range (-20~60°C).

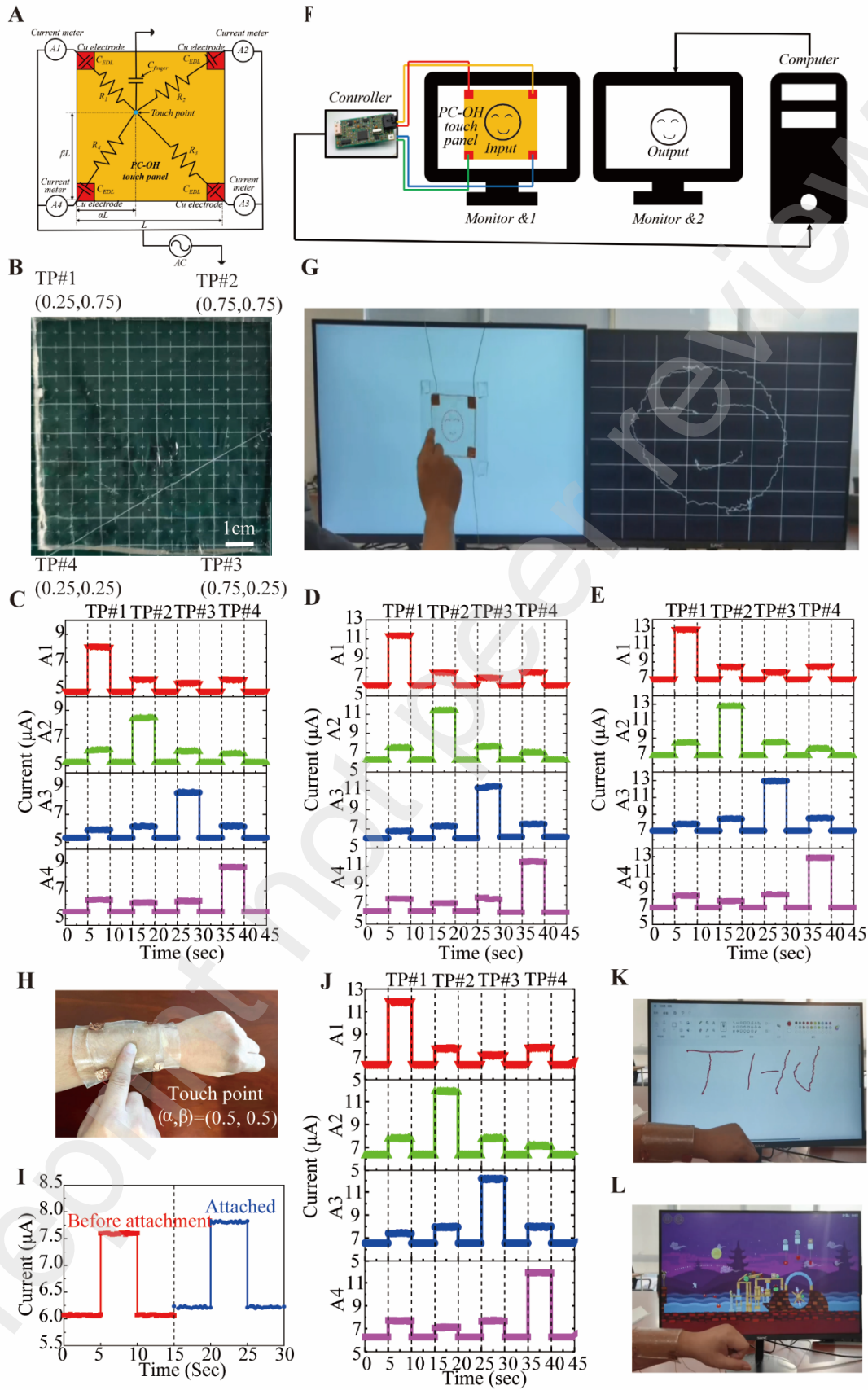


Figure 7. Position sensing and operation of a 2D PC-OH touch panel. (A) The illustration of the PC-OH touch panel, where α and β represent the two normalized distances of the touch position. (B) Optical photograph of the transparent PC-OH touch panel. The sensitivity of position detection can be seen by studying the panel's four touchpoints (TP#1 ~ TP#4). By touching TP#1 ~ TP#4 successively, and using four current meters A1, A2, A3, and A4 to measure the change in currents I1, I2, I3, and I4 with time at different temperatures of -20°C (C), 25°C (D), and 60°C (E). (F) The touch panel is integrated with a desktop through a control board to form a touch system. (G) The function of the touch panel is detected by drawing a smiling face. (H) The touch panel is attached to the human arm. (I) The A1 current of the panel before and after the arm attachment is recorded. (J) The position sensitivity after attachment is studied by measuring A1, A2, A3, and A4 currents at different touch points. The wearable touch panel can detect actions such as clicking, holding, dragging, and swiping. The ability of the touch panel for writing text (K) and playing computer games (L) was demonstrated.

To ensure electrical insulation of the PC-OH panel, we affix it to a larger square PMMA board. The opposite side of the PMMA board is then securely fastened to the display. Copper electrodes are strategically placed at the four corners of the PC-OH panel, subsequently connecting them to a control board. This control board is responsible for generating identical phase AC currents (± 3 V, 17 kHz) at each corner. The real-time currents—namely, I1, I2, I3, and I4—are continuously monitored and converted into digital signals by the control board. When a user's finger touches the touch panel (Figure 7F), these digital signals are transmitted to the computer. The computer processes these signals to calculate and display the coordinates of the touch position on the screen, allowing for real-time interaction with the touch panel. Notably, we conducted tests by drawing a smiling face and concentric square on the integrated touch panel (Figure 7G; Movies S2 and Figure S3, Supporting Information). However, it's important to mention that there may be some distortion at the edges of the output image, owing to the nonlinearity of the 2D touch panel resistances. Additionally, we assessed the touch panel's functionality in wet environments (Movie S4, Supporting Information). For instance, by pouring water on the touch panel and subsequently tracing the pattern behind

the PC-OH, a nearly identical concentric circle can be drawn on the touch screen. Furthermore, our touch panel demonstrates self-healing capabilities. We initially drew a concentric circle on the touch panel by tracing the pattern behind the PC-OH. Subsequently, we introduced a crack in the PC-OH, only to reconnect the resulting pieces for self-healing. Impressively, after a 24-hour healing period, we were able to recreate the nearly identical concentric circle pattern ([Movies S5](#) and [S6](#), Supporting Information). These outcomes underscore the high operational reliability and mechanical flexibility of the PC-OH touch panel under ultra-high stretch conditions, wide temperature ranges (-20~60°C), wet environments, and even when subjected to damage. Expanding on the 2D PC-OH touch panel sensing mechanism, we have innovated the design of a wearable touch panel. In this groundbreaking wearable configuration, we attach a 2.0 mm thick PC-OH film to a 1.0 mm thick highly adhesive (VHB) film. This arrangement effectively isolates the PC-OH touch panel from direct contact with human skin ([Figure 7H](#)). Copper electrodes are then meticulously positioned at each corner of the PC-OH touch panel and subsequently connected to a computer. The resultant wearable touch panel excels in transparency, softness, and stretchability, rendering it comfortable for body-worn use. Moreover, it seamlessly transmits optical information from the touch panel. To assess its performance, we conducted measurements both before and after affixing the wearable touch panel to the human arm ([Figure 7I](#)). Our observations revealed a minor increase in baseline current (from 1 μ A to 2 μ A) attributable to the leakage current passing from the touch panel to the human body through the VHB substrate. Subsequently, we conducted tests in which touchpoints TP#1 to TP#4 on the wearable touch panel were sequentially activated. Current meters provided real-time readings of A1, A2, A3, and A4 currents. Impressively, the results indicated that the relationship between the measured currents and touch positions remained unaffected by the attachment ([Figure 7J](#)). The wearable touch panel demonstrated its ability to flawlessly detect various user gestures, including tapping, holding, dragging, and swiping. This capability not only facilitated user interactions but also allowed for the wearable touch panel to be comfortably worn on the body for activities such as writing ([Figure 7K](#); [Movie S7](#), Supporting Information), drawing ([Figure S7](#) and [Movie. S8](#), Supporting Information), and gaming ([Figure 7L](#) and [Movie. S9](#), Supporting Information).

Discussion

In this study, we have introduced PC-OH organic hydrogel, a novel and versatile material with remarkable adhesion properties and touch-sensing capabilities. The PC-OH hydrogel leverages a combination of multiple interactions, including hydrogen bonding, electrostatic interactions, catechol chemistry, and covalent bonding, to exhibit strong adhesion to various substrates, both in air and underwater. Its ability to adhere to diverse materials, including plastics, paper, glass, stone, steel, and even human skin, highlights its potential for a wide range of applications, particularly in the field of flexible wearable ionic electronics. Quantitative assessment of adhesion strength through lap shear tests revealed impressive results, with high adhesive strengths measured for stone/skin, paper/skin, and glass/skin interfaces. The unique ability of the PC-OH hydrogel to maintain strong adhesion, even in the presence of excess water, underscores its suitability for applications involving exposure to liquids like sweat and rain. Furthermore, the PC-OH hydrogel demonstrates its exceptional performance in touch-sensing applications. Whether in 1D or 2D touch sensors, the hydrogel exhibited reliable position-sensing capabilities, maintaining stability across a wide temperature range and in various environmental conditions, including wetness and damage. Its integration into wearable touch panels showcased its potential for real-time interaction, demonstrating actions such as tapping, holding, dragging, and swiping. The wearable touch panel could comfortably adhere to human skin, making it a promising candidate for applications in e-skin and human-computer interaction.

The PC-OH organic hydrogel's remarkable adhesion properties can be attributed to its rich functional groups, including phenolic hydroxyl groups in TA and active-NHS groups in AA-NHS ester. These functional groups enable a wide range of noncovalent interactions with substrates, such as ion-dipole, metal coordination bonds, and hydrogen bonds. Additionally, dynamic metal coordination bonds and hydrogen bonds within the hydrogel dissipate energy during the peeling process, enhancing its adhesion strength. This synergistic effect of chemical interactions and energy dissipation is particularly advantageous for soft electronic systems operating in humid conditions, where traditional adhesives often struggle to maintain reliability. The hydrogel's exceptional touch-sensing capabilities arise from its resistive nature and the ability to divide the touch panel

into virtual resistive sections. The measured currents at various touchpoints allowed for accurate position detection, making it suitable for a wide range of interactive applications. The hydrogel's self-healing properties further enhance its durability and reliability, ensuring continued functionality even after damage. The integration of the PC-OH hydrogel into a wearable touch panel opens up exciting possibilities for human-computer interaction. Its transparency, softness, and stretchability make it comfortable for extended use, and its ability to detect various user gestures offers versatility in applications ranging from text input to gaming. In summary, the PC-OH organic hydrogel presents a unique combination of adhesion properties and touch-sensing capabilities, making it a promising material for the development of flexible wearable electronics, e-skin, and interactive technologies. Future research may focus on optimizing the hydrogel performance for specific applications and exploring its potential in emerging fields such as healthcare, augmented reality, and human-machine interfaces.

Materials and Methods

Materials: Gelatin ($\geq 99.5\%$, ~250 g Bloom), acrylic acid *n*-hydroxysuccinimide ester (AA-NHS, $\geq 90\%$), tannic acid (TA, 95 %), aluminum chloride hexahydrate ($\text{AlCl}_3 \cdot \text{H}_2\text{O}_2$, 99.99 %), and α -ketoglutaric acid (98 %) were procured from the Aladdin Industrial Corporation (Shanghai, China). Acrylic acid N-hydroxysuccinimide ester (AA-NHS ester, $\geq 90\%$) and gelatin methacrylate (GelMA, bloom 250, degree of substitution 60 %) were obtained from Sigma-Aldrich (Shanghai, China). Glycerol ($\geq 99.5\%$) was sourced from General Reagent (Shanghai, China). All materials were used as received without further purification. Milli-Q ($18.2 \text{ M}\Omega \cdot \text{cm}^{-1}$) was used for all experiments.

Preparation of PC-OH: The PC-OH organic hydrogel, based on P (AA-co-AAm, PC), was synthesized through a three-step process. In the first step, a precursor solution was prepared by mixing gelatin (10 %, w/w), acrylic acid (30 %, w/w), AA-NHS ester (1 %, w/w), TA (0.15 %, w/w), $\text{AlCl}_3 \cdot \text{H}_2\text{O}_2$ (3 %, w/w), α -ketoglutaric acid (0.4 %, w/w), and GelMA (0.1 %, w/w) in Milli-Q water ($\text{M}\Omega \cdot \text{cm}^{-1}$). The solution was stirred with a magnetic stirrer at 65 °C for 2 hours to ensure uniform dispersion. The second step involved curing the precursor solution. The well-mixed solution was poured into two rectangular poly(methyl methacrylate) (PMMA) molds (dimensions: length 100.0 mm, width 100.0 mm, thickness 1.0 mm) separated by silicone pieces (height = 2.0 mm) and then cooled for 30 minutes. Subsequently, the mold was exposed to a UV chamber with an intensity of 10 mW/cm² for 40 minutes for thorough photopolymerization, resulting in the gelatin-PAA-based hydrogel (PC-H). The final step entailed immersing the obtained PC-H in a Milli-Q water/glycerol binary solvent (1:1, v/v) for 4 hours to produce the Gelatin-PAA-based organic hydrogel (PC-OH).

Similarly, a PC-based hydrogel (PC-H) precursor solution was prepared by mixing the aforementioned solutes in Milli-Q water ($\text{M}\Omega \cdot \text{cm}^{-1}$), followed by stirring at 65 °C for 2 hours to ensure uniform dispersion. The clarified mixture solution was then poured into two rectangular poly(methyl methacrylate) (PMMA) molds (dimensions: length 100.0 mm, width 100.0 mm, thickness 1.0 mm) separated by silicone pieces (height = 2.0 mm). After cooling for 30 minutes, the mold was exposed to a UV chamber with an intensity of 10 mW/cm² for 40 minutes to achieve complete photopolymerization, yielding the PAA-based hydrogel (PA-H). Finally, PAA-based organic hydrogel (PA-OH) was prepared by

immersing the obtained PA-H in a Milli-Q water/glycerol binary solvent (1:1, v/v) for 4 hours.

Characterizations: To characterize the properties of the organic hydrogel (PC-OH), freeze-dried gels were subjected to microstructure imaging and infrared spectroscopy using SEM (GeminiSEM 50, Zeiss) and FTIR spectrometer (iS50, Nicolet) with the attenuated total reflectance (ATR) method in the spectral range of 4000-400 cm⁻¹, respectively. The anti-freezing performance of the gels was evaluated using differential scanning calorimetry (TGA/DSC 2, Mettler-Toledo) with a heating rate of 5 °C/min in the temperature range of -60 ~ 60 °C under an air atmosphere. UV-Vis-NIR spectrophotometry (Cary 5000, Agilent) was employed to measure the transmittance of the gel samples with a wavelength range from 400 to 800 nm. Anti-dehydration tests were conducted at 25 °C and 60% relative humidity (RH) with gel samples of 2.0 mm thickness, using air as the reference for measuring transparency. To assess the environmental stability of PC-OH organic hydrogel, the humidity-controlled cabinet was set at 38 % RH, and the temperature was maintained at 25 °C. All samples were initially sized at 40.0 × 20.0 × 2.0 mm, and their weight was measured daily for 7 consecutive days using an electronic scale. The remaining weight ratios of the samples were calculated using the formula m/m₀, where m₀ represents the original weight of the gel samples and m is the weight of gel samples after specific days of storage.

Electromechanical Properties: Digital photographs were taken with a Nikon D90 camera of samples subjected to various mechanical deformations (including stretching, bending, and twisting) after being stored at different conditions (-20 °C, 25 °C, and 60 °C) for 24 hours. Tensile tests were performed using a tension testing machine system (5985, Instron) on strip samples (dimensions: 40.0 × 20.0 × 2.0 mm) with a crosshead distance of 5.0 mm, stretched at a constant speed of 30.0 mm/min. The samples were stored at -20°C, 25°C, or 60°C for at least 24 hours before testing. For low-temperature tests, a -20 °C cooling chamber surrounded the sample to maintain it at -20 °C during stretching. Similarly, for high-temperature tests, a heating chamber surrounded the sample to maintain it at 60 °C during stretching. The modulus of the samples was determined from the slope of the stress-strain curve in the strain range of 0 % to 10 %. The strain was calculated as $\epsilon = (l-l_0)/l_0 \times 100 \%$, where l₀ is the initial gauge length, and

l is the length after deformation. Tensile stress (σ) was calculated using $\sigma = F/A_0$, with A_0 representing the initial cross-sectional area and F the tensile load.

Ionic conductivities of the materials were obtained from complex impedance plots measured using an electrochemical workstation (PARSTAT 4000A, Princeton) in the frequency range of 0.1 Hz to 1 MHz with an alternating-current sine wave amplitude of 200 mV. Cylindrical PC-OH samples (diameter: 12.0 mm, depth: 2.0 mm) were sandwiched between two round steel electrodes. The bulk resistance (R_b) of the materials was determined by fitting the intercept of the real axis of the Nyquist plot at a high frequency using Z-view software. The conductivity of stretchable PC-OH was calculated as $\sigma = L/(A \cdot R_b)$, where L corresponds to the distance between the electrodes, and A denotes the cross-sectional area of the sample.

Adhesive Test: The lap shear test was conducted to assess the adhesion properties of PC-OH organic hydrogel at the interface between various substrate surfaces (plastic, paper, glass, stone, steel, and rubber) and the PC-OH organic hydrogel. Rectangular PC-OH organic hydrogel samples (dimensions: 30.0 mm \times 30.0 mm \times 2.0 mm) were attached between the surfaces of two substrates. Subsequently, the samples were pulled at a fixed speed of 10.0 mm/min until separation using a tensile machine (5985, Instron) under ambient conditions. The adhesive strength was calculated by dividing the maximum load by the initial adhesion area, while adhesion energy was determined by dividing two times the plateau force by the width of the specimen. To further characterize the adhesion performance of PC-OH under different conditions, adhered specimens were subjected to lap shear tests at different temperatures (-20 °C, room temperature of 25 °C, and high temperature of 60 °C) and in humid environments, including underwater conditions. In these tests, polyethylene terephthalate (PET) films and cyanoacrylate adhesives were used as stiff backing and substrates for PC-OH organic hydrogels.

Self-healing Tests: Before testing, the samples were stored at a predetermined temperature (-20 °C, 25 °C, or 60 °C) for at least 12 hours. To study the mechanical properties of self-healed PC-OH organic hydrogel, the samples were cut into two pieces, and the sections were joined together and stored for at least 24 hours to facilitate self-healing. The mechanical properties of the self-healed sample were then tested using a universal material testing machine (5985, Instron). The time-dependent self-healing

process was observed using an optical microscope (BX 53, Olympus). Samples were cut with a sharp knife and the cut surfaces gently rejoined in the air. To measure the direct current (DC) before and after self-healing of the PC-OH sample, a PC-OH strip (dimensions: $4.0 \times 2.0 \times 0.1$ cm) was connected to a current meter (Model 34461A, Agilent). A DC voltage of 3.0 V was applied to the PC-OH strip using a function generator (Model 33612A, Agilent). The touch strip was cut into two pieces with a sharp ceramic knife, and the currents were recorded over time throughout the process.

Biocompatibility Test in vitro: In vitro, biocompatibility testing of PC-OH was performed using the 3-(4,5-dimethylthiazol-2-yl)-2,5-diphenyltetrazolium bromide (MTT) assay (CCK-8 kit, Yeasen, Guangzhou, China). The optical density (OD) value at 450 nm was measured using an enzyme marker to indirectly reflect the number of viable cells. A piece of PC-OH organic hydrogel (2.0 g) was immersed in 10 mL of deionized water for 24 h at room temperature. A549 cells were plated in a 96-well plate (2000 cells/well) with six parallel wells ($n=6$). The cells were cultured in Dulbecco's Modified Eagle Medium (DMEM) medium (HyClone, USA) and complete growth medium with 10 % fetal bovine serum, 100 U mL⁻¹ penicillin, and 0.1 mg/mL streptomycin (Thermo Fisher Scientific, USA) at 37 °C in 5 % CO₂. After 12 hours of cell culture, 100 µL of PC-OH organic hydrogel extract was added to the medium. The cells were then incubated at 37 °C for 24 h, 48 h, and 72 h. CCK-8 (10 µL), which comprised 10 % of the total medium volume, was added and incubated for 2 h in the dark. The OD value was measured at 450 nm using a microplate reader (Tecan Microplate Reader Spark, USA). For fluorescence imaging, cells were incubated with PC-OH hydrogel extract for 24 h, then stained with 2 µg mL⁻¹ Calcein-AM (Biolab, China), incubated in the dark for 30 min in an incubator, and washed three times with PBS. After adding the medium, images were captured using a confocal fluorescence microscope (Nikon A1R SI confocal, Japan).

In vitro, biocompatibility testing of deionized water and PAA-hydrogel-conditioned medium was used as a control.

1D Touch Strip: A PC-OH touch strip ($10.0 \times 3.0 \times 0.2$ cm) was made, and copper electrodes (1.0×1.0 cm) and a current meter (multimeter, model 34461A, Agilent) were connected to the two ends of the touch strip. A function generator (model 33612A,

Agilent) was connected to the two parallel current meters, and an AC current of the same phase was applied to both sides of the PC-OH strip. The strip was touched with a finger to show the relationship between touch position and current, which was recorded by the current meters at each touch point. The strips were then stretched to twice their original length and touched with a finger in stretch mode. In these cases, the measured currents were recorded at temperatures of -20 °C, 25 °C, and 60 °C with an AC voltage of -3.0 ~ 3.0 V at a frequency of 17 kHz generated by the function generator. Unless otherwise stated, the samples in this study were stored at the test temperature for at least 12 hours. To study the sensing ability of the touch strip in a wet environment, the touch strip was sprayed with water and then allowed to air dry for a different time, resulting in different levels of wetness (wet, dampish, and recovery). To study the electrical self-healing ability of the touch strip, it was also cut with a sharp ceramic knife, and the freshly cut parts were rejoined.

The Sensing Mechanism of the 1D Touch Strip: To investigate its sensing mechanism, a 1D touch strip was employed due to its simplification of the current flow description within the PC-OH touch sensing system. This model incorporates two resistors and three capacitors for the severed and reconnected strip. When a human finger makes contact with the strip, current can traverse from the copper electrodes to the ground through the strip. The touch position enables the calculation of resistance values for the two resistors:

$$R_1 = \alpha R + R_l \quad (1)$$

$$R_2 = (1 - \alpha R) + R_r \quad (2)$$

where R represents the total resistance of the uncut strip, and α signifies the normalized position. Additionally, R_l and R_r denote the additional resistances introduced by the incompletely healed interface between the touch point and the current meters A1 and A2, respectively. Each resistor is in series with a capacitor C_{EDL} . Consequently, the impedance Z for both segments can be calculated as follows:

$$Z_1 = R_1 - j \frac{1}{2\pi f C_{EDL}}, \quad Z_2 = R_2 - j \frac{1}{2\pi f C_{EDL}} \quad (3)$$

Since the capacitance per unit area of the double layer C_{EDL} is about 10^{-1} F/m^2 ; the area of the double layer is about $6 \times 10^{-5} \text{ m}^2$, and the current frequency is around 17 kHz, the reactance of the double layer is $-j \frac{1}{2\pi f C_{EDL}} \approx -1.6j$. As this reactance is much smaller

than the resistance of the PC-OH touch strip ($R \sim 3300 \Omega$, $T = 25^\circ\text{C}$), the impedance is $Z = 3300\Omega - 1.6j \approx 3300\angle - 0.028$ and can be approximated by the resistance value ($Z \approx R$) so that the ratio of the two resistances can be used to calculate the touch current. The voltages on the two resistor parts are:

$$U_1 = I_1 \cdot Z_1 \approx I_1 \cdot R_1 \approx \alpha I_1 \cdot R + I_1 \cdot R_l = (\alpha + k_1)I_1 \cdot R \quad (4)$$

$$U_2 = I_2 \cdot Z_2 \approx I_2 \cdot R_2 \approx (1 - \alpha)I_2 \cdot R + I_2 \cdot R_r = (1 - \alpha + k_2)I_2 \cdot R \quad (5)$$

where K_1 and K_2 are the ratios of the healing interface-induced additional resistance, which is related to the total resistance of the uncut strip.

The two resistance parts are in parallel connection, and the voltages U_1 and U_2 on the two resistances are the same with $K_1 = K_2$, thereby:

$$(\alpha + k_1)I_1 \cdot R = (1 - \alpha + k_2)I_2 \cdot R \quad (6)$$

$$\alpha = \frac{I_2}{I_t} + \frac{K_2 I_2 - K_1 I_1}{I_t} \quad (7)$$

where I_t is the circuit's current, and I_t can be expressed as $I_t = I_1 + I_2$.

The original and electrically completely recovered strip with:

$$K_1 = K_2 = 0 \quad (8)$$

$$\alpha = \frac{I_2}{I_t} \quad (9)$$

2D Touch Panel: The 2D touch panel setup involved connecting each corner of the PC-OH touch panel ($8.0 \times 8.0 \times 0.2$ cm) to a copper electrode, which was subsequently linked to the controller board via copper wires. To ensure precise functionality, we utilized the MT 7 software control panel (version 7.14.9) as a calibration tool, provided by the controller board manufacturer. Initially, when the 2D PC-OH touch panel was first used, the output figures were not suitable for display. To enhance touch accuracy, we performed a three-point calibration.

Wearable Touch Panel: A wearable touch panel was created using VHB™ 4910 tape as an insulator. The PC-OH touchpad was affixed to a VHB film, and copper electrodes were connected to its four corners. This assembled wearable touch panel can be comfortably attached to the human body without compromising its functionality. When placed on the human arm, the wearable touch panel remains entirely transparent, allowing for visibility of the arm beneath it and enabling seamless operation. To power this setup, a function generator supplied an AC voltage ranging from -0.3 to 0.3V at a

frequency of 17kHz.

It's essential to note that the study protocol underwent a comprehensive review and received approval from the ethical committee of the Tsinghua Shenzhen International Graduate School, Tsinghua University (Number 2023-F088).

Preprint not peer reviewed

Acknowledgments

This work is supported by National Key Research and Development Program of China (2023YFA0913600), National Natural Science Foundation of China (31970752, 22278242), China Postdoctoral Science Foundation (2023M730856), Shenzhen Excellent Scientific and Technological Innovation Talent Training Program (RCBS20221008093129082), Science, Technology, Innovation Commission of Shenzhen Municipality (JCYJ20190809180003689, JSGG20200225150707332, JCYJ20220530143014032, KCXFZ20211020163813019, ZDSYS20200820165400003, WDZC20200820173710001, WDZC20200821150704001, JSGG20191129110812708), Shenzhen Bay Laboratory Open Funding (SZBL2020090501004, SZBL2021080601011) Department of Chemical Engineering-iBHE Cooperation Joint Fund Project (DCE-iBHE-2022-3), Tsinghua Shenzhen International Graduate School Cross-disciplinary Research and Innovation Fund Research Plan (JC2022009), Bureau of Planning, Land and Resources of Shenzhen Municipality (2022-207).

Author contributions:

Conceptualization: Z. L. C., J. Q. Y., D. M. Y., P. W. Q., C. Y. Z., Methodology: Z. L. C., L. K. Z., Z. Y. L., C. H. Y., Y. Z., Investigation: Q. H. S., L. L. X., Visualization: X. P. Z., Y. C. W., K. L., Supervision: D. M. Y., P. W. Q., C. Y. Z., Writing: Z. L. C., J. Q. Y., Writing & Review & Editing: D. M. Y., P. W. Q., C. Y. Z.

Competing interests: All other authors declare they have no competing interests.

Data and materials availability: All data are available in the main text or the supplementary materials.

References

- [1] Z. Chen, F. Li, L. Zhang, Z. Lei, C. Yang, C. Xiao, L. Lian, X. Yuan, G. Ijaz, J. Yang, Z. Lin, Y. He, P. Zhang, D. Yu, P. Qin, *Chemical Engineering Journal* **2023**, *451*, 138672.
- [2] G. Gao, F. Yang, F. Zhou, J. He, W. Lu, P. Xiao, H. Yan, C. Pan, T. Chen, Z. L. Wang, *Advanced Materials* **2020**, *32*, 2004290.
- [3] C. C. Kim, H. H. Lee, K. H. Oh, J. Y. Sun, *Science (1979)* **2016**, *353*, 682.
- [4] C. Han, F. Yang, X. Guo, Y. Bai, G. Liu, H. Sun, P. Wang, W. Liu, R. Wang, *Adv Mater Interfaces* **2021**, *8*, 2100742.
- [5] X. Guo, F. Yang, X. Sun, Y. Bai, G. Liu, W. Liu, R. Wang, X. He, *Adv Funct Mater* **2022**, *32*, 2201230.
- [6] X. Guo, F. Yang, W. Liu, C. Han, Y. Bai, X. Sun, L. Hao, W. Jiao, R. Wang, *J Mater Chem A Mater* **2021**, *9*, 14806.
- [7] B.-J. Cheon, J.-W. Kim, M.-C. Oh, *Opt Express* **2013**, *21*, 4734.
- [8] M. Takasaki, H. Kotani, T. Mizuno, T. Nara, in *2005 IEEE/RSJ International Conference on Intelligent Robots and Systems, IROS*, IEEE, **2005**, pp. 3354–3359.
- [9] M. C. Brenner, J. J. Fitzgibbon, *J Acoust Soc Am* **1988**, *84*, 1578.
- [10] H. Hoshyarmanesh, N. Nehzat, M. Salehi, M. Ghodsi, H. S. Lee, H. H. Park, *Materials and Manufacturing Processes* **2014**, *29*, 870.
- [11] Z. Cui, A. Huang, J. Chen, S. Gao, *IEEE Sens J* **2021**, *21*, 26389.
- [12] H. Park, S. J. Oh, D. Kim, M. Kim, C. Lee, H. Joo, I. Woo, J. W. Bae, J. H. Lee, *Advanced Science* **2022**, *9*, 2201070.
- [13] Y. Lee, S. Lim, W. J. Song, S. Lee, S. J. Yoon, J. M. Park, M. G. Lee, Y. L. Park, J. Y. Sun, *Advanced Materials* **2022**, *34*, 2108586.
- [14] Z. Chen, B. Cotterell, W. Wang, *Eng Fract Mech* **2002**, *69*, 597.
- [15] S. Yang, E. Ng, N. Lu, *Extreme Mech Lett* **2015**, *2*, 37.
- [16] S. Yoon, Y. J. Kim, Y. R. Lee, N. E. Lee, Y. Won, S. Gandla, S. Kim, H. K. Kim, *NPG Asia Mater* **2021**, *13*, 1.
- [17] K. McLellan, Y. Yoon, S. N. Leung, S. H. Ko, *Adv Mater Technol* **2020**, *5*, 1900939.
- [18] C. Ma, H. Luo, M. Liu, H. Yang, H. Liu, X. Zhang, L. Jiang, *Chemical Engineering Journal* **2021**, *425*, 131542.
- [19] H. Yu, Y. Tian, M. Dirican, D. Fang, C. Yan, J. Xie, D. Jia, Y. Liu, C. Li, M. Cui, H. Liu, G. Chen, X. Zhang, J. Tao, *Carbohydr Polym* **2021**, *273*, 118539.
- [20] Y. Yan, L. Wei, X. Qiu, J. Shao, H. Liu, X. Cui, J. Huang, L. Xie, Z. Hu, C. Huang, *ACS Appl Polym Mater* **2021**, *3*, 1479.
- [21] Y. W. Lee, S. Chun, D. Son, X. Hu, M. Schneider, M. Sitti, *Advanced Materials* **2022**, *34*, 2109325.
- [22] B. Grigoryan, S. J. Paulsen, D. C. Corbett, D. W. Sazer, C. L. Fortin, A. J. Zaita, P. T. Greenfield, N. J. Calafat, J. P. Gounley, A. H. Ta, F. Johansson, A. Randles, J. E. Rosenkrantz, J. D. Louis-Rosenberg, P. A. Galie, K. R. Stevens, J. S. Miller, *Science (1979)* **2019**, *364*, 458.
- [23] H. Zhang, H. Xu, W. Sun, X. Fang, P. Qin, J. Huang, J. Fang, F. Lin, C. Xiong, *Acta Biomater* **2023**, *159*, 38.
- [24] V. M. Kadiri, C. Bussi, A. W. Holle, K. Son, H. Kwon, G. Schütz, M. G. Gutierrez, P. Fischer, *Advanced Materials* **2020**, *32*, 2001114.
- [25] G. Khandelwal, T. Minocha, S. K. Yadav, A. Chandrasekhar, N. P. M. J. Raj, S. C. Gupta, S.-J. Kim, *Nano Energy* **2019**, *65*, 104016.
- [26] R. Guo, Y. Fang, Z. Wang, A. Libanori, X. Xiao, D. Wan, X. Cui, S. Sang, W. Zhang, H. Zhang, J. Chen, *Adv Funct Mater* **2022**, *32*, 2204803.
- [27] Y. Wang, Y. Xia, P. Xiang, Y. Dai, Y. Gao, H. Xu, J. Yu, G. Gao, K. Chen, *Chemical Engineering Journal* **2022**, *428*, 131171.
- [28] A. Beck, F. Obst, D. Gruner, A. Voigt, P. J. Mehner, S. Gruenzner, R. Koerbitz, M. H. Shahadha, A. Kutscher, G. Paschew, U. Marschner, A. Richter, *Adv Mater Technol* **2022**, 2200417.
- [29] Y. Zhang, C. K. Jeong, J. Wang, X. Chen, K. H. Choi, L. Q. Chen, W. Chen, Q. M. Zhang, Q. Wang, *Advanced Materials* **2021**, *33*, 2103056.
- [30] Z. Xu, F. Zhou, H. Yan, G. Gao, H. Li, R. Li, T. Chen, *Nano Energy* **2021**, *90*, 106614.

- [31] H. Dinh Xuan, B. Timothy, H. Y. Park, T. N. Lam, D. Kim, Y. Go, J. Kim, Y. Lee, S. Il Ahn, S. H. Jin, J. Yoon, *Advanced Materials* **2021**, *33*, 2008849.
- [32] B. Yang, Y. Zhao, M. U. Ali, J. Ji, H. Yan, C. Zhao, Y. Cai, C. Zhang, H. Meng, *Advanced Materials* **2022**, *34*, 2201342.
- [33] Z. Jiang, P. Song, *Science (1979)* **2022**, *376*, 245.
- [34] C. Y. Lo, Y. Zhao, C. Kim, Y. Alsaad, R. Khodambashi, M. Peet, R. Fisher, H. Marvi, S. Berman, D. Aukes, X. He, *Materials Today* **2021**, *50*, 35.
- [35] K. Cho, D. Kang, H. Lee, W. G. Koh, *Chemical Engineering Journal* **2022**, *427*, 130879.
- [36] D. Fan, X. Yuan, W. Wu, R. Zhu, X. Yang, Y. Liao, Y. Ma, C. Xiao, C. Chen, C. Liu, H. Wang, P. Qin, *Nat Commun* **2022**, *13*, 5083.
- [37] Z. Zhang, Z. Yao, Y. Li, S. Lu, X. Wu, Z. Jiang, *Chemical Engineering Journal* **2022**, *433*, 134488.
- [38] A. Heiden, D. Preninger, L. Lehner, M. Baumgartner, M. Drack, E. Woritzka, D. Schiller, R. Gerstmayr, F. Hartmann, M. Kaltenbrunner, *Sci Robot* **2022**, *7*, eabk2119.
- [39] Y. Xu, Q. Rong, T. Zhao, M. Liu, *Giant* **2020**, *2*, 100014.
- [40] Y. Niu, H. Liu, R. He, M. Luo, M. Shu, F. Xu, *Small* **2021**, *17*, 2101151.
- [41] X. Zhang, C. Cui, S. Chen, L. Meng, H. Zhao, F. Xu, J. Yang, *Chemistry of Materials* **2022**, *34*, 1065.
- [42] B. Ying, R. Z. Chen, R. Zuo, J. Li, X. Liu, *Adv Funct Mater* **2021**, *31*, 2104665.
- [43] X. Sui, H. Guo, C. Cai, Q. Li, C. Wen, X. Zhang, X. Wang, J. Yang, L. Zhang, *Chemical Engineering Journal* **2021**, *419*, 129478.
- [44] J. Wang, Y. Huang, B. Liu, Z. Li, J. Zhang, G. Yang, P. Hiralal, S. Jin, H. Zhou, *Energy Storage Mater* **2021**, *41*, 599.
- [45] Y. Chen, X. Guo, A. Mensah, Q. Wang, Q. Wei, *ACS Appl Mater Interfaces* **2021**, *13*, 59761.
- [46] M. Guo, X. Yang, J. Yan, Z. An, L. Wang, Y. Wu, C. Zhao, D. Xiang, H. Li, Z. Li, H. Zhou, *J Mater Chem A Mater Chem* **2022**, *10*, 16095.
- [47] C. Lu, J. Qiu, W. Zhao, E. Sakai, G. Zhang, R. Nobe, M. Kudo, T. Komiya, *Int J Biol Macromol* **2021**, *188*, 534.
- [48] L. J. Hawkins, M. Wang, B. Zhang, Q. Xiao, H. Wang, K. B. Storey, *Comp Biochem Physiol Part D Genomics Proteomics* **2019**, *30*, 1.
- [49] Y. Feng, J. Yu, D. Sun, W. Ren, C. Shao, R. Sun, *Chemical Engineering Journal* **2022**, *433*, 133202.
- [50] P. Shi, Y. Wang, W. W. Tjiu, C. Zhang, T. Liu, *ACS Appl Mater Interfaces* **2021**, *13*, 49358.
- [51] X. F. Zhang, X. Ma, T. Hou, K. Guo, J. Yin, Z. Wang, L. Shu, M. He, J. Yao, *Angewandte Chemie - International Edition* **2019**, *58*, 7366.
- [52] C. Xie, X. Wang, H. He, Y. Ding, X. Lu, *Adv Funct Mater* **2020**, *30*, 1909954.
- [53] E. Wieschaus, R. Riggleman, *Cell* **1987**, *49*, 177.
- [54] C. Capitain, S. Wagner, J. Hummel, N. Tippkötter, *Waste Biomass Valorization* **2021**, *12*, 1761.